

Article

Pt-Fe-Co Ternary Metal Single Atom Catalyst for toward High Efficiency Alkaline Oxygen Reduction Reaction

Ruimin Zhang, Ke Wang, Peng Wang *, Yan He * and Zhiming Liu * 

Shandong Engineering Laboratory for Preparation and Application of High-Performance Carbon-Materials, College of Electromechanical Engineering, Qingdao University of Science & Technology, Qingdao 266061, China; zrmzgzq1997@163.com (R.Z.); wk980306@163.com (K.W.)

* Correspondence: pengwangmse@qust.edu.cn (P.W.); heyanyan@qust.edu.cn (Y.H.); zmliu@qust.edu.cn (Z.L.)

Abstract: Single-atom catalysts (SACs) within carbon matrix became one of the most promising alternatives to noble metal-based catalysts for oxygen reduction reaction (ORR). Although SACs have significant benefits in reducing the total catalyst cost, it also has the disadvantages of weak interaction between atoms and poor stability. Hence, there is still much room for improvement for the catalyst activity. In response, we designed a Fe-Co-Pt ternary metal single atom catalyst anchored on covalent organic framework (COF)-derived N-doped carbon nanospheres (Pt, Fe, Co/N-C). Due to effective charge transfer between Pt single atom and neighboring Fe-Co components, an intense electron interaction can be established within the Pt, Fe, Co/N-C catalyst. This is beneficial for enhancing charge transfer efficiency, modulating d electronic structure of Pt center and weakening oxygen intermediate adsorption, thus distinctly accelerating ORR catalytic kinetics. As expected, the half-wave potential of Pt, Fe, Co/N-C was 0.845 V, much higher than those of commercial 20 wt% Pt/C (0.835 V), Pt/N-C (0.79 V) and Fe, Co/N-C (0.81 V) counterparts. Moreover, the Pt, Fe, Co/N-C catalyst demonstrated much-improved cycling stability and methanol tolerance.

Keywords: oxygen reduction reaction; electrocatalysts; single atom; ternary metal; kinetics



Citation: Zhang, R.; Wang, K.; Wang, P.; He, Y.; Liu, Z. Pt-Fe-Co Ternary Metal Single Atom Catalyst for toward High Efficiency Alkaline Oxygen Reduction Reaction. *Energies* **2023**, *16*, 3684. <https://doi.org/10.3390/en16093684>

Academic Editor: Roger Gläser

Received: 23 March 2023

Revised: 20 April 2023

Accepted: 24 April 2023

Published: 25 April 2023



Copyright: © 2023 by the authors. Licensee MDPI, Basel, Switzerland. This article is an open access article distributed under the terms and conditions of the Creative Commons Attribution (CC BY) license (<https://creativecommons.org/licenses/by/4.0/>).

1. Introduction

The consumption of fossil fuels and related environmental pollution recently attracted more and more attention. Therefore, the development of clean and sustainable energy became an important research topic. Oxygen reduction reaction (ORR) is a key process in many modern energy conversion and storage devices, such as fuel cells, water electrolyzers and rechargeable metal–air batteries [1–9]. In such devices, the overall reaction rate is generally limited by the ORR dynamics, and each reaction rate involves a cooperative four-electron–four-proton electrocatalytic reaction [10,11]. So, the development of efficient ORR electrocatalysts is essential to promote the reaction rates and stimulate the widespread deployment of electrochemical energy systems [12,13]. So far, platinum- (Pt) and Pt-based materials are considered to be the most active ORR electrocatalysts [14–17]. However, the high cost and poor stability of these noble metal catalysts seriously hindered their large-scale application in real-world devices. Today, non-noble-metal and metal-free electrocatalysts for ORR are also attracting attention due to their outstanding stability. However, when compared with those Pt-based ORR catalysts, the catalytic activity is still not satisfactory [18–20]. Therefore, in recent decades, the research was devoted to simultaneously reducing the cost and enhancing the catalytic activity of platinum-based catalyst by reducing Pt dimension or introducing non-precious transition metal component [21].

In particular, metal-separated single atomic sites catalysts attracted much attention due to their ultimate atom utilization efficiency and excellent catalytic performance [21–24]. In particular, atomically dispersed metal sites fixed in nitrogen-doped carbon matrix (M-N-C) are considered to be the most promising ORR catalysts. Specially, due to plenty

of metal active sites with unsaturated coordination structure and robust M-N interaction, those M-N-C catalysts can usually provide largely ameliorated ORR catalytic activity and stability when compared with those of metal-free electrocatalysts [25–27]. However, the single atom catalyst also has some disadvantages, that is, on account of isolated spatial distribution, the disorderly dispersed single sites make less use of synergistic effect among adjacent metal sites and, thus, lack of electronic coupling. As a result, the further catalytic activity improvement of M-N-C catalyst is undesirably limited. Therefore, the development of double-monatomic and triple-monatomic catalysts can not only maintain the high catalytic activity of atomically dispersed catalyst, but also the introduction of multi metals can directly regulate the d-band electronic structure and local coordination environment of metal sites. This is beneficial for motivating catalytic efficiency of each metal site and achieving the optimal adsorption strength towards oxygen-containing intermediates during ORR. Hence, double-monatomic and triple-monatomic catalysts will provide a new opportunity to regulate the electronic and geometric structure of M-N-C catalysts. For example, Cao et al. demonstrated that Fe and Co porphyrins can work well as bi-functional ORR/OER electrocatalysts for rechargeable zinc-air batteries [28]. Fu et al. reported that two monatomic catalyst sites of Cu-N₄ and Zn-N₄ modified on N-doped carbon substrate also showed excellent ORR activity [29]. These findings give us a good inspiration to further arrange double non-noble metal single atoms pairs around the Pt single atoms to realize the synergistic effect between them. Therefore, it is of great significance to rationally design the synthesis route and optimize the support structure to control the content, distribution and valence state of the three metals and significantly improve the catalytic performance of Pt-based catalyst. It is highly desirable but full of challenges.

Apart from metal components, different carbon substrates, including graphene, carbon nanotubes, metal-organic frameworks (MOFs)-derived carbon and so on, also play crucial roles in enhancing the whole catalytic activity of M-N-C composite. In particular, due to their outstanding chemical and thermal stability, COFs-derived carbon materials showed a wide range of applications in gas absorption, ion conduction, heterogeneous catalysis, membrane science, energy storage and conversion since the concept of COFs was initially proposed by Yaghi's group [30–34]. For example, Li et al. demonstrated the use of Fe single atom anchored within COF-derived carbon can distinctly ameliorate ORR kinetics [35]. It is mentioned that, in contrast to MOFs, covalent organic framework materials are metal-free. Therefore, it is easier to characterize and determine the catalytic effect of the metal single atoms anchored on the N-doped carbon derived from the COF, effectively avoiding the influence of metal impurities on the carrier.

Herein, we issued a fresh “COF absorption-pyrolysis” strategy to fabricate Pt-Fe-Co ternary metal single atom catalyst in the present work. First, nano-COF spheres were synthesized by solution method. Then, the as-obtained COF spheres precursor was fully adsorbed with Co atoms, Fe atoms and Pt atoms. The introduction of Fe, Co components aims to optimize the local coordination environment and electron distribution of Pt single atom centers. Finally, Pt, Fe, Co/N-C was obtained after high temperature annealing. X-ray diffraction (XRD) and high-resolution transmission electron microscopy (HRTEM) identified no metal particles were on the surface of carbon nanospheres matrix. Additionally, the X-ray photoelectron spectroscopy (XPS) characterizations further conclude that Fe, Co atoms can efficiently modulate the valence state and electronic structure of Pt center via efficient charge transfer from Fe, Co to Pt. As expected, the Pt, Fe, Co/N-C catalyst showed better ORR catalytic performance in alkaline medium with a half-wave potential of 0.85 V, even 10 mV higher than the commercial 20 wt% Pt/C. Furthermore, the Pt, Fe, Co/N-C catalyst also showed outstanding long-term stability and superior methanol tolerance. The excellent electrocatalytic performance is mainly attributed to electronic synergy effect between Fe, Co components and noble Pt single atom, which may efficiently optimize the d-band center and, thus, the oxygen intermediates adsorption capability of Pt catalytic centers. Our work may provide an alternative approach for the design of high-performance noble metal atom-based catalysts.

2. Materials and Methods

2.1. Materials

1,3,5-tri (4-aminophenyl) benzene (97%), 1,3,5-phenyltriformaldehyde (97%), glacial acetic acid (AR, 99.5%), Cobalt (II) acetate tetrahydrate ($\text{Co}(\text{Ac})_2 \cdot 4\text{H}_2\text{O}$, 99.5%), Iron(III) chloride hexahydrate ($\text{FeCl}_3 \cdot 6\text{H}_2\text{O}$, 99%), Chloroplatinic acid hexahydrate ($\text{H}_2\text{PtCl}_6 \cdot 6\text{H}_2\text{O}$, Pt 37.5%) and KOH were purchased from Aladdin Chemical Reagent Co., Ltd. Methanol (AR), ethanol (AR) were purchased from Sinopharm Chemical. Commercial Pt/C (20 wt%) and Nafion solution (5 wt%) were purchased from Sigma-Aldrich. The distilled water was homemade by ion exchange and filtration.

2.2. Preparation of COF [35]

An amount of 205 mg 1,3,5-tri (4-aminophenyl) benzene, 95 mg 1,3,5-benzaldehyde were added into 60 mL ethanol at room temperature. After 5 min of vigorously stirring at 700 rpm on a magnetic mixer, 6 mL glacial acetic acid was added. Then, the mixture was vigorously stirred for another 15 min. Finally, the COF powders were collected by double centrifugation at 13,500 rpm for six minutes, respectively. The N-C products were then dried at 50 °C for 3–5 h.

2.3. Preparation of Pt, Fe, Co/N-C

An amount of 30 mg COF powders were dissolved in 10 mL acetonitrile. Then, 500 μL $\text{Co}(\text{Ac})_2 \cdot 4\text{H}_2\text{O}$ aqueous solution (5 mg mL^{-1}), 500 μL $\text{FeCl}_3 \cdot 6\text{H}_2\text{O}$ aqueous solution (5 mg mL^{-1}) and 200 μL $\text{H}_2\text{PtCl}_6 \cdot 6\text{H}_2\text{O}$ aqueous solution (5 mg mL^{-1}) were added to the above solution and vigorously stirred for 24 h at 70 °C. After full absorption of metals ions, the powders were collected by centrifugation at 13,500 rpm for six minutes and dried at 80 °C for 5 h. Then, the obtained powders were heated to 900 °C at the heating rate of 5 °C min^{-1} and underwent a simple annealing at 900 °C for 3 h under inert AR atmosphere, achieving Pt,Fe,Co/N-C powders after naturally cooling to room temperature.

2.4. Preparation of Fe, Co/N-C

The process parameters were similar to those of Pt,Fe,Co/N-C except for with the absence of 200 μL $\text{H}_2\text{PtCl}_6 \cdot 6\text{H}_2\text{O}$ aqueous solution (5 mg mL^{-1}) and stirring at room temperature.

2.5. Preparation of Pt/N-C

The process parameters were similar to those of Pt,Fe,Co/N-C except for with the absence of 500 μL $\text{Co}(\text{Ac})_2 \cdot 4\text{H}_2\text{O}$ aqueous solution (5 mg mL^{-1}), 500 μL $\text{FeCl}_3 \cdot 6\text{H}_2\text{O}$ aqueous solution (5 mg mL^{-1}).

2.6. Preparation of N-C

The process parameters were similar to those of Pt,Fe,Co/N-C except for with the absence of 500 μL $\text{Co}(\text{Ac})_2 \cdot 4\text{H}_2\text{O}$ aqueous solution (5 mg mL^{-1}), 500 μL $\text{FeCl}_3 \cdot 6\text{H}_2\text{O}$ aqueous solution (5 mg mL^{-1}) and 200 μL $\text{H}_2\text{PtCl}_6 \cdot 6\text{H}_2\text{O}$ aqueous solution (5 mg mL^{-1}).

2.7. Materials Characterizations

The morphologies of the samples were characterized by scanning electron microscopy (SEM, Hitachi SU-8010, Tokyo, Japan) and high resolution transmission electron microscopy (HRTEM, FEI Tecnai G2 F30, Hillsboro, OR, USA). The crystalline structure information was confirmed by X-ray diffraction technique (XRD, Rigaku MiniFlex-600, Tokyo, Japan) with $\text{Cu-K}\alpha$ radiation. Raman spectra were measured on an In Via Reflex Raman spectroscopy with a laser source of 532 nm. The surface elemental composition and valence state were determined by X-ray photoelectron spectroscopy (XPS, Thermo Scientific K-Alpha, Waltham, MA, USA). The specific surface and pore size distributions of Bruno–Emmett–Taylor (BET) were obtained from the Beishide 3H-2000 PS/PM system by nitrogen adsorption–desorption isotherm method.

2.8. Electrocatalytic Measurements

Electrochemical measurements were performed using a three-electrode system in an O₂-saturated 0.1 M KOH solution at room temperature at CHI 760E Electrochemical Workstation (CHI Instruments, Shanghai, China). The polished glassy carbon rotating disk electrode (RDE) or rotating ring disk electrode (RRDE) with a Pt ring (4 mm inner diameter), graphite rod and saturated calomel electrode (SCE) were used as working electrode, counter electrode and reference electrode, respectively. All the characterized catalysts were prepared by mixing 5 mg catalyst and 1 mg super P in a mixture containing 380 μ L ethanol, 100 μ L water and 20 μ L 5 wt% Nafion solution. Then, the catalyst solutions were ultrasonic mixed for several hours to get homogeneous catalyst ink. Then, 7 μ L of non-noble metal catalyst ink was carefully dripped onto the working electrode to ensure that the electrode was completely covered. After being dried at room temperature, the resulting non-noble metal catalyst loading was about 0.56 mg cm². In addition, 4 μ L commercially 20 wt% of Pt/C catalyst ink was dripped on the working electrode, and the resulting loading was about 0.32 mg cm².

Before the electrochemical test, a catalyst activation experiment was conducted by CV cycle between 0.3 and 0.8 V at 50 mV s⁻¹. Polarization curves were recorded by linear sweep voltammetry (LSV) at room temperature with a scan rate of 10 mV s⁻¹ and 95% IR compensation. In addition, according to Nernst equation, ORR potentials were normalized to reversible hydrogen electrode (RHE). E (vs. RHE) = E (SCE) + 0.0591 * pH + 0.244. Linear sweep voltammetry (LSV) measurements were performed at various speeds in the range of 400–2500 rpm with a sweep speed of 10 mV s⁻¹. The electrochemical double layer capacitance (C_{dl}) was measured by typical cyclic voltammetry (CV) at different scanning rates (10, 20, 40, 60 and 80 mV s⁻¹) at 0.9–1.1 V compared with RHE. Then, the electrochemical surface area (ECSA) was calculated according to the C_{dl} values. In the hydrogen peroxide yield test, the disk electrode of RRDE was scanned at a rate of 10 mV s⁻¹, and the ring electrode potential was set to 1.23 V vs. RHE. The yield of hydrogen peroxide (H₂O₂) and electron transfer were calculated according to the following formula (n):

$$\text{H}_2\text{O}_2 (\%) = 200 \times \frac{I_r}{I_d + I_r} \cdot N$$
$$n = 4 \times \frac{I_d}{I_d + I_r} \cdot N$$

In the above equation, I_d and I_r are disk current and ring current, respectively, and N is the current collection efficiency of platinum ring, whose value was 0.4.

The durability of the catalysts was tested in 0.1 M KOH solution saturated with O₂, and the voltage was set corresponding to the limiting current density in the i-T test. Additionally, methanol tolerance was tested in 0.1 M KOH oxygen-saturated solution containing 1 M methanol.

3. Results and Discussion

3.1. Design and Characterizations of Catalysts

The synthesis procedure is illustrated in Figure 1. First, a simple solvent method was used to obtain COF carriers at room temperature [35]. 1,3,5-tri (4-aminophenyl) benzene and 1,3,5-phenyltriformaldehyde were stirred to mix in ethanol solution. Then, glacial acetic acid solution was added to catalyze the Schiff base reaction later. Then, yellow COF solids were obtained after washing by centrifugation and drying. Additionally, then, a small amount of Pt, Fe, Co ions and the yellow solids were dispersed into the acetonitrile solution for further mixing. During the stirring process, the metal ions would coordinate with the N atoms in the resulting precursor. After stirring for 24 h at room temperature, yellow solids were obtained by centrifugation and drying. It is mentioned that the nano-COF spheres with uniform size distribution and morphology can promote the absorption of precursor metal ions, which is beneficial for improving the interface contact between catalytic active site and carbon substrate. Then, the Pt, Fe, Co/N-C catalyst could be

achieved after calcination at high temperature under inert atmosphere, during which the coordination strength between Pt, Fe, Co atoms and N atom within COF precursor could be distinctly enhanced, making Pt, Fe, Co atoms exist as single atom pattern.



Figure 1. Synthesis process of Pt, Fe, Co/N-C.

As shown in SEM and TEM images Figure 2a,b, the synthetic COF-derived carbon nanospheres in the Pt, Fe, Co/N-C catalyst were uniformly dispersed with diameters of about 150 nm. As shown in Figure S1, the diameters of carbon nanospheres in Fe, Co/N-C, Pt/N-C and N-C were similar to the carbon nanospheres in Pt, Fe, Co/N-C. This means that the introduction of three metal atoms within in carbon substrate had a negligible effect on the morphology and size of carbon nanospheres, which is beneficial not only for guaranteeing the stability of carbon skeleton but also promoting the uniform distribution and sufficient exposure of metal sites. Then, the nitrogen adsorption–desorption results in Figure S2 and pore size distribution profiles in Figure S3 confirm the Pt, Fe, Co/N-C composite possess large specific surface area of $710.38 \text{ m}^2 \text{ g}^{-1}$ and abundant micropores. Herein, the well-defined Pt, Fe, Co/N-C catalyst with excellent surface area and robust porous framework facilitates the high-speed mass/electron transport and adequate electrolyte infiltration. Additionally, as seen from Figure 2c, there were no metal particles of iron, cobalt and platinum observed on the smooth surface of the carbon nanospheres in Pt, Fe, Co/N-C. Meanwhile, the corresponding selected area electron diffraction (SAED) result (Figure 2d) further excludes the existence of crystalline metal nanoparticles on the surface of Pt, Fe, Co/N-C. Furthermore, as shown in the high-angle annular dark field scanning TEM (HAADF-STEM) in Figure 2e, no agglomerated metal particles with brighter contrast can be discerned, further eliminating the existence of Pt, Fe, Co nanoparticles or nanoclusters. It can be concluded that the COF-derived carbon sphere was strongly chelated with the metal atom to avoid the aggregation into the cluster or nanoparticles. According to the HRTEM and SAED pictures, we believe that Fe, Co and Pt can exist in the form of single atom. As shown in Figure 2f, the corresponding energy dispersive X-ray spectrogram shows the homogeneous distribution of carbon, iron, cobalt and platinum elements within the whole carbon skeleton.

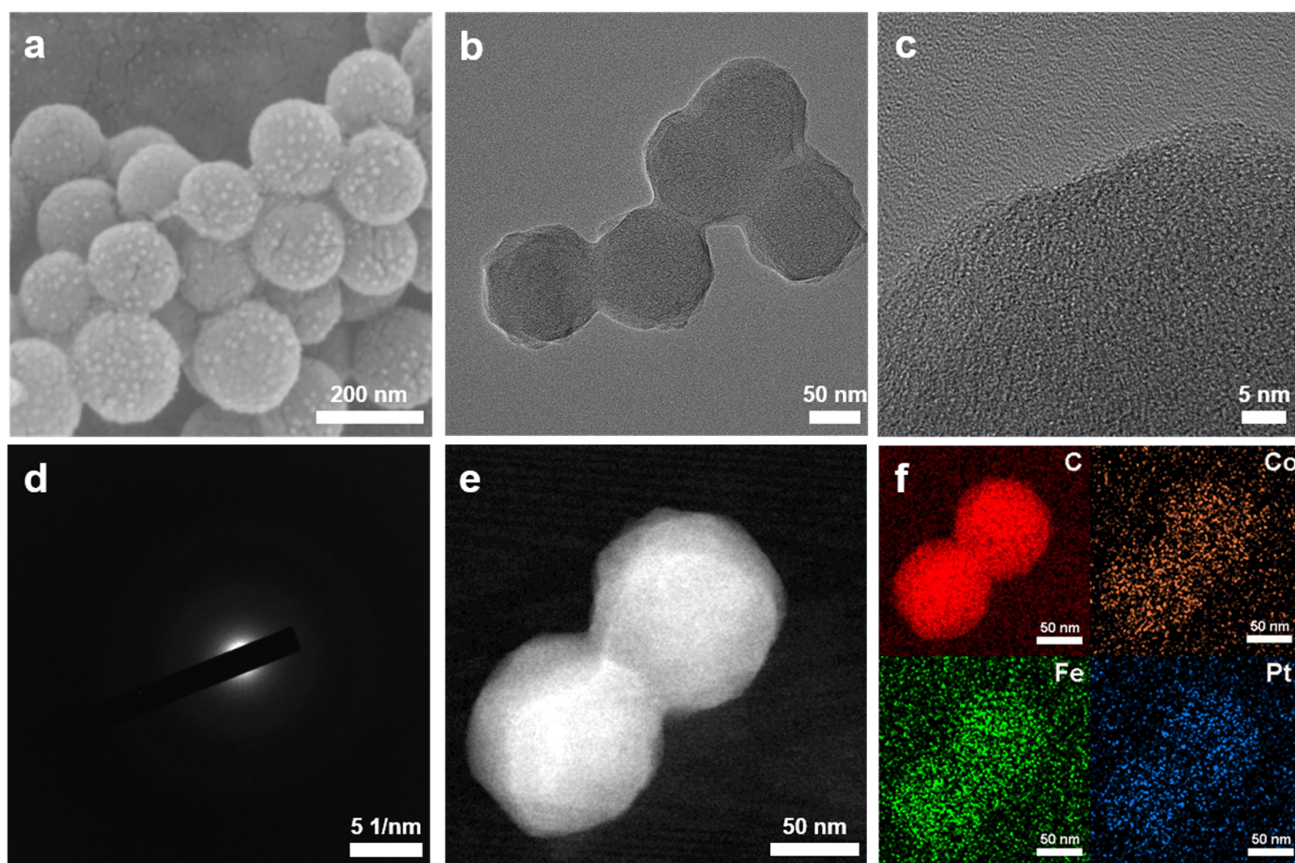


Figure 2. (a) SEM image of Pt, Fe, Co/N-C; (b) TEM image of Pt, Fe, Co/N-C; (c) HRTEM image of Pt, Fe, Co/N-C; (d) SAED map of Pt, Fe, Co/N-C; (e) HAADF-STEM image of Pt, Fe, Co/N-C; (f) Corresponding energy dispersive X-ray spectroscopy elemental mapping results of Pt, Fe, Co/N-C.

To better understand the structure of Pt, Fe, Co/N-C, we performed X-ray diffraction (XRD) and Raman characterizations. We can see from the XRD profiles (Figure 3a) that all the Pt/N-C, N-C, Pt, Fe, Co/N-C and Fe, Co/N-C catalysts had the characteristic peaks of carbon, and no characteristic peaks of metals nanoparticles were detected, which is consistent with HRTEM and SAED results [36]. The X-ray photoelectron spectroscopy (XPS) spectra of Pt, Fe, Co/N-C (Figure S4) are mainly comprised of Fe, Co, Pt, C, N and O elements. As shown in Figure S5, the high-resolution C 1s XPS spectra of Pt, Fe, Co/N-C, Fe, Co/N-C and Pt/N-C were fitted into three peaks, attributed to C-C, C-O and C=O, respectively. The high-resolution N 1s XPS spectrum (Figure 3b) indicates the presence of pyridine-N (~398.4 eV), pyrrolic N (~399.6 eV), the dominated graphitic N (~401.0 eV) and oxidized N (~402.8 eV) in Pt, Fe, Co/N-C, Fe, Co/N-C and Pt/N-C [37]. It is mentioned that the content of pyridine nitrogen will increase with the addition of iron and cobalt ions, indicating the intense coordination effect between pyridine nitrogen and metal ions. Both the high-resolution Co 2p and Fe 2p spectra signals of Pt, Fe, Co/N-C, Fe, Co/N-C were too weak (Figure 3c,d), which was possibly due to the trace loading of Fe, Co species beyond the detection sensitivity. This further discloses the single atom nature of Fe, Co atoms within in carbon sphere matrix. Importantly, as shown in Figure 3e, the peaks located at 72.0 and 75.3 eV can be identified as $\text{Pt}^{2+} 4f_{7/2}$ and $\text{Pt}^{2+} 4f_{5/2}$, respectively. According to the binding energies, it can be seen that the Pt element was positively charged, indicating its oxidation state. This further indicates the single-atom pattern of Pt component in the Pt, Fe, Co/N-C catalyst [38]. It is mentioned that compared with that of Pt/N-C, the peak of Pt in Pt, Fe, Co/N-C was significantly shifted to the right, indicating that the valence state of Pt was reduced, which further indicates that there was an apparent charge transfer between Pt and Fe-Co single-atoms. The charge transfer from Fe and Co to Pt is

conductive to the establishment of a strong synergistic effect between precious metals and non-precious metals. According to the reported literatures, the electrons obtainment of Pt atom can induce the negatively shifting of its d-band center, which make its anti-bonding orbital is filled with electrons. This is beneficial for weakening the adsorption towards oxygen-involved intermediates and thus accelerating the catalytic kinetics of ORR [39]. In addition, we analyzed the XPS data to determine the element composition of the materials, as shown in Table S1.

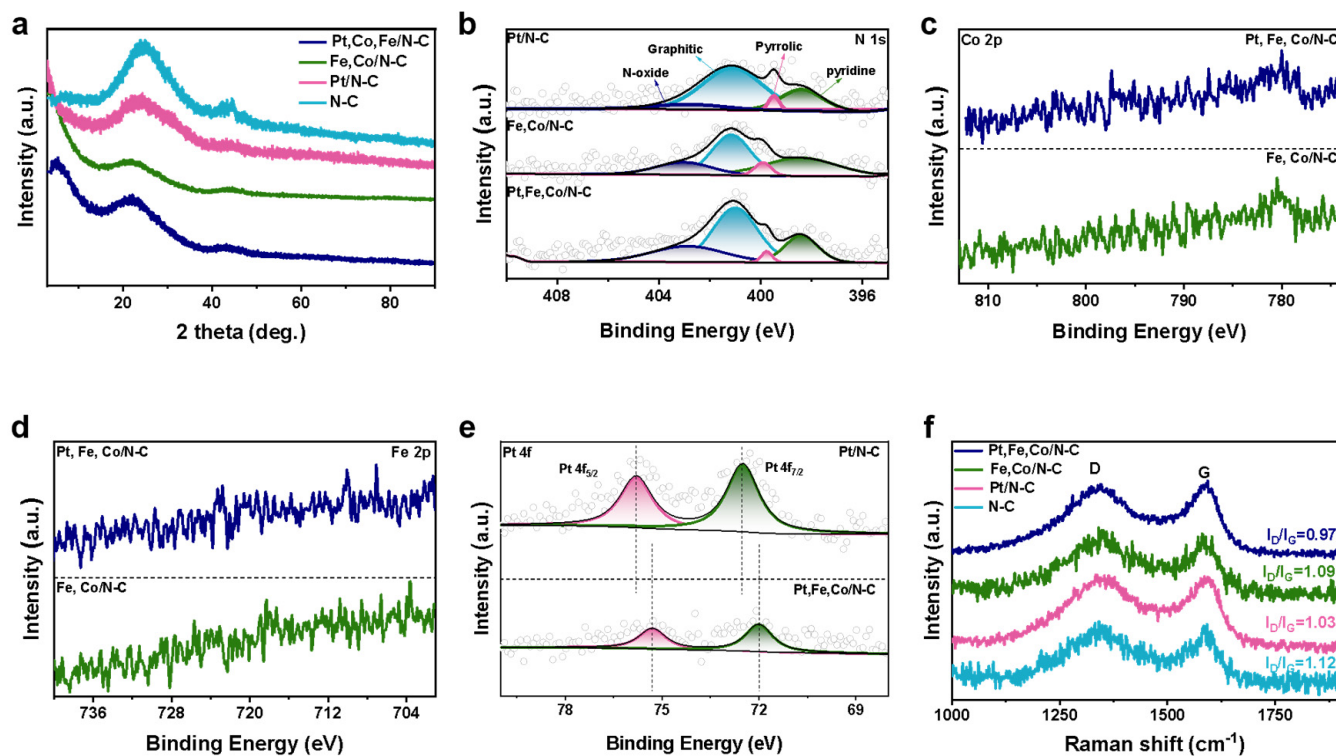


Figure 3. (a) XRD data of N-C and Pt, Fe, Co/N-C and Fe, Co/N-C, Pt/N-C; (b) XPS spectra of N 1s in the sample of Pt, Fe, Co/N-C and Fe, Co/N-C, Pt/N-C; (c) XPS spectra of Fe 2p in the sample of Pt, Fe, Co/N-C and Fe, Co/N-C; (d) XPS spectra of Co 2p in the sample of Pt, Fe, Co/N-C and Fe, Co/N-C; (e) XPS spectra of Pt 4f in the sample of Pt, Fe, Co/N-C and Pt/N-C; (f) Raman spectra of the N-C and Pt, Fe, Co/N-C and Fe, Co/N-C, Pt/N-C.

Furthermore, as shown in the Raman spectra in Figure 3f, in comparison to that of pure N-C, after the addition of Pt and Fe, Co atoms, the ratio of I_D/I_G of the metal atom functionalized carbon catalysts decreased, which means that with the chelated metal atoms, the surface defects of carbon matrix can be distinctly passivated, contributing to the enhancement of long-period stability. At the same time, the I_D/I_G ratios of Pt, Fe, Co/N-C and Pt/N-C, Fe, Co/N-C were very different, which also confirm the interaction between Pt and Fe, Co atoms. Based on these analysis results, it was confirmed that Fe, Co and Pt exist in the form of single atom in the COF-derived carbon matrix, constructing ternary metal single atom catalyst. Moreover, the electronic interaction between Pt single atoms and Fe-Co single atoms contributes to the change of the coordination environment and electron distribution around the active Pt sites. As a result, this well-designed structure can be expected to provide superior activity driving force centers for alkaline ORR, thus distinctly boosting the ORR reaction kinetics.

3.2. Electrocatalytic Performances

We tested ORR activities of Pt, Fe, Co/N-C using a three-electrode system in an oxygen-saturated 0.1 M potassium hydroxide solution. First, the ORR catalytic performances of all the catalysts were tested by linear sweep voltammetry (LSV) at 1600 rpm. As shown in

Figure 4a,b, the Pt, Fe, Co/N-C catalyst exhibited the best ORR catalytic performance with a more positive half wave potential ($E_{1/2} = 0.845$ V) and higher dynamic current density at 0.85 V ($J_k = 4.37$ mA cm⁻²) than those of commercial 20 wt% Pt/C ($E_{1/2} = 0.835$ V, $J_k = 2.31$ mA cm⁻²). In sharp contrast, the pure N-C catalyst had the worst ORR catalytic performance, with a half-wave potential of only 0.72 V, fully demonstrating the critical role of metal single atoms in improving ORR catalytic kinetics. Meanwhile, in order to prove the unique role of the interaction between Pt atom and Fe, Co atoms, the electrocatalytic performances of comparison samples of Fe, Co/N-C and Pt/N-C were also tested. The half-wave potentials of Fe, Co/N-C and Pt/N-C are 0.81 V and 0.79 V, respectively. These results indicate that the main active sites and activity origin for ORR catalysis are governed by different metal sites, instead of the N-C substrate. Moreover, Fe, Co and Pt interact with each other to change the coordination environment and electron distribution, thus promoting the catalytic performance of ORR.

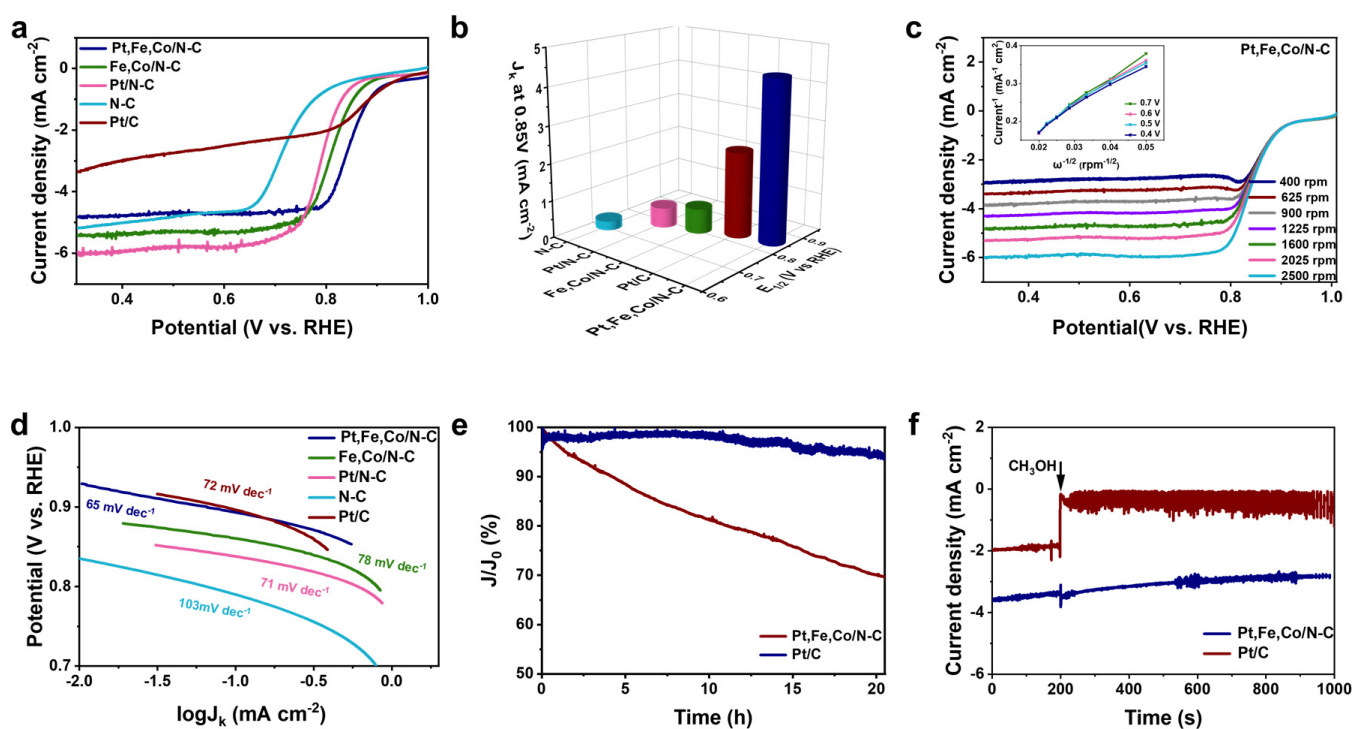


Figure 4. (a) ORR polarization curves for different catalysts of Pt, Fe, Co/N-C, Fe, Co/N-C and Pt/N-C, N-C, 20 wt% Pt/C; (b) J_k at 0.85 V and $E_{1/2}$ of Pt, Fe, Co/N-C, Fe, Co/N-C and Pt/N-C, N-C, 20 wt% Pt/C; (c) ORR polarization curves at different rotating rates of Pt, Fe, Co/N-C. The inset in (c) is the Koutecky–Levich plots of Pt, Fe, Co/N-C catalyst at different applied potentials; (d) the comparison of the Tafel slopes of Pt, Fe, Co/N-C, Fe, Co/N-C and Pt/N-C, N-C, 20 wt% Pt/C; (e) chronoamperometric (i-t) curves for Pt, Fe, Co/N-C; (f) tolerance to methanol of Pt, Fe, Co/N-C.

We can also see from the CV profiles in Figure S6, in comparison to those of Fe, Co/N-C, Pt/N-C, N-C and 20 wt% Pt/C, the Pt, Fe, Co/N-C catalyst showed a more positive oxygen reduction peak, which was further consistent with its larger half-wave potentials, further indicating its much-ameliorated ORR catalytic efficiency. Then, Figure 4c and Figure S7 show the ORR catalytic performance of Pt, Fe, Co/N-C and contrast sample at different rotational speeds tested by LSV, respectively. In order to further clarify the ORR reaction mechanism of the Pt, Fe, Co/N-C catalyst, Figure 4c was further analyzed by virtue of the Koutecky–Levich equation, and the number of transferred electrons N was calculated to be 3.94, equal to about 4, indicating that this Pt, Fe, Co/N-C catalyst possessed a high selectivity for four-electron process. We also evaluated the ORR catalytic performance using a rotating ring electrode test to obtain the number of transferred electrons and the H₂O₂ yield. As shown in Figure S8, the n value for Pt, Fe, Co/N-C was almost 4 in the

range of 0.3–0.9 V, with the lowest H₂O₂ yields ranging from 3% to 15%. Therefore, the ORR process catalyzed by Pt, Fe, Co/N-C is a four-electron process, which proves that Fe, Co and Pt do have positive interactions. As shown in Figure 4d, the Tafel slopes of all the catalysts were calculated, where the value for Pt, Fe, Co/N-C was 65 mV dec⁻¹, which is lower than Fe, Co/N-C (78 mV dec⁻¹), Pt/N-C (71 mV dec⁻¹), N-C (103 mV dec⁻¹) and 20 wt% Pt/C (72 mV dec⁻¹), furthering confirming the advantage of the Pt, Fe, Co/N-C hybrid in enhancing the ORR kinetics. It can be inferred that thanks to this d–d electron interaction between different metal centers, the charge transfer efficiency can be distinctly improved. Meanwhile, d electron structure of Pt center can also be optimized, facilitating weakening the adsorption strength of oxygen intermediates. These factors synergistically contribute to accelerating the alkaline ORR catalytic reaction kinetics.

Then, the electrochemical active surface area (ECSA) of these catalysts was measured by electrochemical double-layer capacitance (C_{dl}) using cyclic voltammetry (Figure S9). The C_{dl} is the half of the slope between the current density difference (Δj) at the potential of 1 V vs. RHE and the scanning rate. As shown in Figure S10, the ECSA value for Pt, Fe, Co/N-C was 48.4 mF·cm⁻², which is far better than those of Fe, Co/N-C (20.5 mV dec⁻¹), Pt/N-C (15.5 mV dec⁻¹) and N-C (2.4 mV dec⁻¹). It indicates Pt, Fe, Co/N-C has the better ECSA, which is also the reason for its much-improved ORR catalytic performance. As shown in Figure 4e, in addition to excellent ORR catalytic performance, the Pt, Fe, Co/N-C hybrid also has excellent long cycle performance. After 20 h of constant voltage test, only 6 percent of the current of Pt, Fe, Co/N-C was lost, indicating its superior cycling stability. In sharp contrast, the benchmark 20 wt% Pt/C catalyst lost about 30% current, signifying its considerably poor stability at the same condition. Furthermore, in order to evaluate the fuel crossover effect, we observed the change of the i-T curve by adding methanol to an O₂-saturated alkaline electrolyte. As shown in Figure 4f, when methanol was added at 200 s, it was found that the current of 20 wt% Pt/C catalyst decreased significantly. The current of Pt, Fe, Co/N-C catalyst did not change much after the fluctuation, which proves that Pt, Fe, Co/N-C catalyst has excellent methanol tolerance. As a result, it can be inferred that based on the solid chelation interaction between the COF-derived carbon nanosphere and metal atoms, the Pt, Fe, Co/N-C catalyst can maintain durable resistance to active sites deactivation and methanol corrosion in alkaline environment. In addition, we assembled self-made zinc–air batteries for electrochemical testing. It can be seen from Figure S11a that the zinc–air battery with Pt, Fe, Co/N-C as negative electrode material has charge and discharge function. Moreover, it can be seen from Figure S11b that the highest power density of the zinc–air battery assembled by Pt, Fe, Co/N-C was 99 mW cm⁻², which is much higher than that of the zinc–air battery assembled by commercial 20 wt% Pt/C catalyst (59.2 mW cm⁻²). The results further show that the Pt, Fe, Co/N-C catalyst has excellent practical application capability.

4. Conclusions

In summary, to solve the inherent limitation of lack of interaction between adjacent atoms of single atom catalyst, we proposed a novel “COF absorption-pyrolysis” strategy to fabricate Pt-Fe-Co ternary metal single atom catalyst. The introduction of transition metal (Fe, Co) ions, which plays critical roles in improving charge transfer efficiency, modulating the electronic structure of Pt center and weakening oxygen intermediate adsorption capability. In addition, the surface chelation mechanism between the COF matrix and Pt, Fe and Co are conducive to the full exposure of the active sites, which can maximize the active site utilization efficiency and speed up the four-electron reaction process of Pt, Fe, Co/N-C. In addition, the solid chelation effect between the COF-derived carbon spheres and metal atoms endows the Pt-Fe-Co/N-C catalyst excellent cycling stability. As expected, excellent ORR catalytic activity was obtained for the Pt-Fe-Co/N-C hybrid. The elaborately-designed Pt, Fe, Co/N-C catalyst achieves a higher half-wave potential of 0.845 V in 0.1 M KOH electrolyte, which is larger than those of 20 wt% Pt/C

(0.835 V), Pt/N-C (0.79 V) and Fe₂Co/N-C (0.81 V). As a proof-of-concept, this work provides a new idea for the rational construction of noble metal oxygen reduction catalyst.

Supplementary Materials: The following supporting information can be downloaded at: <https://www.mdpi.com/article/10.3390/en16093684/s1>, Figure S1. The SEM images of comparison samples. (a) Pt/N-C, N-C, (b) Fe, Co/N-C, (c) N-C. Figure S2. Nitrogen adsorption-desorption isotherms of Pt, Fe, Co/N-C and Fe, Co/N-C, Pt/N-C, N-C. Figure S3. Pore size distributions of Pt, Fe, Co/N-C and Fe, Co/N-C, Pt/N-C, N-C. Figure S4. XPS survey spectrum of Pt, Fe, Co/N-C and Fe, Co/N-C, Pt/N-C. Figure S5. XPS C 1s spectra of Pt, Fe, Co/N-C and Fe, Co/N-C, Pt/N-C. Figure S6. CV curves of Pt, Fe, Co/N-C, Fe, Co/N-C, Pt/N-C, N-C and Pt/C in an O₂-saturated 0.1 M KOH solution. Figure S7. ORR polarization curves at different rotating rates of comparison samples. (a) Fe, Co/N-C, (b) Pt/N-C (c) N-C and (d) Pt/C. Figure S8. The number of transferred electrons and H₂O₂ yield of Pt, Fe, Co/N-C, Fe, Co/N-C, Pt/N-C, Pt/C and N-C. Figure S9. Scan rate dependence of current densities in CV curves for different samples. (a) Pt, Fe, Co/N-C, (b) Fe, Co/N-C, (c) Pt/N-C and (d) N-C. Figure S10. The C_{dl} curves of Pt, Fe, Co/N-C, Fe, Co/N-C, Pt/N-C, and N-C. Figure S11. (a) Charge-discharge curves of Pt, Fe, Co/N-C and 20 wt% Pt/C; (b) Discharge polarization and power density curves of Pt, Fe, Co/N-C and 20 wt% Pt/C. Table S1. Materials elemental composition.

Author Contributions: Conceptualization, K.W.; Data curation, R.Z.; Writing—original draft, R.Z.; Writing—review & editing, P.W.; Project administration, Y.H. and Z.L.; Funding acquisition, Y.H. and Z.L. All authors have read and agreed to the published version of the manuscript.

Funding: This work was funded by the National Natural Science Foundation of China (Grant Nos. 21905152 and 52176076), the Taishan Scholar Project of Shandong Province of China (Grant Nos. tsqn202211160 and ts20190937), the Youth Innovation Team Project for Talent Introduction and Cultivation in Universities of Shandong Province, and the China Postdoctoral Science Foundation (Grant Nos. 2022M713249).

Data Availability Statement: All data employed in this work can be available from the corresponding author upon.

Conflicts of Interest: The authors declare no conflict of interest.

References

1. Seh, Z.W.; Kibsgaard, J.; Dickens, C.F.; Chorkendorff, I.B.; Norskov, J.K.; Jaramillo, T.F. Combining theory and experiment in electrocatalysis: Insights into materials design. *Science* **2017**, *355*, eaad4998. [[CrossRef](#)] [[PubMed](#)]
2. Sun, R.; Guo, W.; Han, X.; Hong, X. Two-dimensional Noble Metal Nanomaterials for Electrocatalysis. *Chem. Res. Chin. Univ.* **2020**, *36*, 597–610. [[CrossRef](#)]
3. Wang, Z.; Lei, Q.; Wang, Z.; Yuan, H.; Cao, L.; Qin, N.; Lu, Z.; Xiao, J.; Liu, J. In-situ synthesis of free-standing FeNi-oxyhydroxide nanosheets as a highly efficient electrocatalyst for water oxidation. *Chem. Eng. J.* **2020**, *395*, 125180. [[CrossRef](#)]
4. Xu, D.; Long, X.; Xiao, J.; Zhang, Z.; Liu, G.; Tong, H.; Liu, Z.; Li, N.; Qian, D.; Li, J.; et al. Rationally constructing CoO and CoSe₂ hybrid with CNTs-graphene for impressively enhanced oxygen evolution and DFT calculations. *Chem. Eng. J.* **2021**, *422*, 129982. [[CrossRef](#)]
5. Sun, H.; Xu, X.; Song, Y.; Zhou, W.; Shao, Z. Designing High-Valence Metal Sites for Electrochemical Water Splitting. *Adv. Funct. Mater.* **2021**, *31*, 2009779. [[CrossRef](#)]
6. Wu, D.; Wei, Y.; Ren, X.; Ji, X.; Liu, Y.; Guo, X.; Liu, Z.; Asiri, A.M.; Wei, Q.; Sun, X. Co(OH)₂ Nanoparticle-Encapsulating Conductive Nanowires Array: Room-Temperature Electrochemical Preparation for High-Performance Water Oxidation Electrocatalysis. *Adv. Mater.* **2018**, *30*, 1705366. [[CrossRef](#)]
7. Ye, C.; Zhang, L.; Yue, L.; Deng, B.; Cao, Y.; Liu, Q.; Luo, Y.; Lu, S.; Zheng, B.; Sun, X. A NiCo LDH nanosheet array on graphite felt: An efficient 3D electrocatalyst for the oxygen evolution reaction in alkaline media. *Inorg. Chem. Front.* **2021**, *8*, 3162–3166. [[CrossRef](#)]
8. Xu, Z.; Zhao, H.; Liang, J.; Wang, Y.; Li, T.; Luo, Y.; Shi, X.; Lu, S.; Feng, Z.; Wu, Q.; et al. Noble-metal-free electrospun nanomaterials as electrocatalysts for oxygen reduction reaction. *Mater. Today Phys.* **2020**, *15*, 100280. [[CrossRef](#)]
9. Xu, X.; Wang, W.; Zhou, W.; Shao, Z. Recent Advances in Novel Nanostructuring Methods of Perovskite Electrocatalysts for Energy-Related Applications. *Small Methods* **2018**, *2*, 1800071. [[CrossRef](#)]
10. Liu, J.; Xiao, J.; Wang, Z.; Yuan, H.; Lu, Z.; Luo, B.; Tian, E.; Waterhouse, G.I.N. Structural and Electronic Engineering of Ir-Doped Ni-(O_{xy})hydroxide Nanosheets for Enhanced Oxygen Evolution Activity. *ACS Catal.* **2021**, *11*, 5386–5395. [[CrossRef](#)]
11. Liu, J.; Zhang, T.; Waterhouse, G.I.N. Complex alloy nanostructures as advanced catalysts for oxygen electrocatalysis: From materials design to applications. *J. Mater. Chem. A* **2020**, *8*, 23142–23161. [[CrossRef](#)]

12. Liu, J.; Zhu, D.; Zheng, Y.; Vasileff, A.; Qiao, S.-Z. Self-Supported Earth-Abundant Nanoarrays as Efficient and Robust Electrocatalysts for Energy-Related Reactions. *ACS Catal.* **2018**, *8*, 6707–6732. [[CrossRef](#)]
13. Liu, J.; Zhu, D.; Guo, C.; Vasileff, A.; Qiao, S. Design Strategies toward Advanced MOF-Derived Electrocatalysts for Energy-Conversion Reactions. *Adv. Energy Mater.* **2017**, *7*, 1700518. [[CrossRef](#)]
14. Jiang, R.; Li, L.; Sheng, T.; Hu, G.; Chen, Y.; Wang, L. Edge-Site Engineering of Atomically Dispersed Fe-N₄ by Selective C-N Bond Cleavage for Enhanced Oxygen Reduction Reaction Activities. *J. Am. Chem. Soc.* **2018**, *140*, 11594–11598. [[CrossRef](#)] [[PubMed](#)]
15. Wu, H.; Wu, J.; Li, Y.; Li, W.; Zhai, J.; Jiang, Q.; Xu, X.; Gao, Y. Enhanced oxygen reduction with carbon-polyhedron-supported discrete cobalt-nitrogen sites for Zn-air batteries. *Chem. Eng. J.* **2022**, *431*, 134084. [[CrossRef](#)]
16. Huang, X.; Zhao, Z.; Cao, L.; Chen, Y.; Zhu, E.; Lin, Z.; Li, M.; Yan, A.; Zettl, A.; Wang, Y.; et al. High-performance transition metal-doped Pt₃Ni octahedra for oxygen reduction reaction. *Science* **2015**, *348*, 1230–1234. [[CrossRef](#)]
17. Nie, Y.; Li, L.; Wei, Z. Recent advancements in Pt and Pt-free catalysts for oxygen reduction reaction. *Chem. Soc. Rev.* **2015**, *44*, 2168–2201. [[CrossRef](#)]
18. Huang, X.; Wang, Y.; Li, W.; Hou, Y. Noble metal-free catalysts for oxygen reduction reaction. *Sci. China Chem.* **2017**, *60*, 1494–1507. [[CrossRef](#)]
19. Zong, M.; Ding, Z.; He, W.; Luo, J.; Tang, Z. Peptide Based Noble Metal Nanomaterials for Oxygen Reduction Reaction: A Review. *Int. J. Electrochem. Sci.* **2020**, *15*, 2634–2647. [[CrossRef](#)]
20. Gao, Y.; Xiao, Z.; Kong, D.; Iqbal, R.; Yang, Q.-H.; Zhi, L. N,P co-doped hollow carbon nanofiber membranes with superior mass transfer property for trifunctional metal-free electrocatalysis. *Nano Energy* **2019**, *64*, 103879. [[CrossRef](#)]
21. Song, Z.X.; Zhu, Y.N.; Liu, H.S.; Banis, M.N.; Zhang, L.; Li, J.J.; Doyle-Davis, K.; Li, R.Y.; Sham, T.K.; Yang, L.J.; et al. Engineering the Low Coordinated Pt Single Atom to Achieve the Superior Electrocatalytic Performance toward Oxygen Reduction. *Small* **2020**, *16*, 12. [[CrossRef](#)] [[PubMed](#)]
22. Li, F.; Li, Y.; Zeng, X.; Chen, Z. Exploration of High-Performance Single-Atom Catalysts on Support M-1/FeOx for CO Oxidation via Computational Study. *ACS Catal.* **2015**, *5*, 544–552. [[CrossRef](#)]
23. Yang, X.-F.; Wang, A.; Qiao, B.; Li, J.; Liu, J.; Zhang, T. Single-Atom Catalysts: A New Frontier in Heterogeneous Catalysis. *Acc. Chem. Res.* **2013**, *46*, 1740–1748. [[CrossRef](#)] [[PubMed](#)]
24. Liu, L.; Corma, A. Metal Catalysts for Heterogeneous Catalysis: From Single Atoms to Nanoclusters and Nanoparticles. *Chem. Rev.* **2018**, *118*, 4981–5079. [[CrossRef](#)] [[PubMed](#)]
25. Zhu, Y.P.; Guo, C.; Zheng, Y.; Qiao, S.-Z. Surface and Interface Engineering of Noble-Metal-Free Electrocatalysts for Efficient Energy Conversion Processes. *Accounts Chem. Res.* **2017**, *50*, 915–923. [[CrossRef](#)]
26. Ito, Y.; Qiu, H.-J.; Fujita, T.; Tanabe, Y.; Tanigaki, K.; Chen, M. Bicontinuous Nanoporous N-doped Graphene for the Oxygen Reduction Reaction. *Adv. Mater.* **2014**, *26*, 4145–4150. [[CrossRef](#)]
27. Dai, L.; Xue, Y.; Qu, L.; Choi, H.-J.; Baek, J.-B. Metal-Free Catalysts for Oxygen Reduction Reaction. *Chem. Rev.* **2015**, *115*, 4823–4892. [[CrossRef](#)]
28. Lv, B.; Li, X.; Guo, K.; Ma, J.; Wang, Y.; Lei, H.; Wang, F.; Jin, X.; Zhang, Q.; Zhang, W.; et al. Controlling Oxygen Reduction Selectivity through Steric Effects: Electrocatalytic Two-Electron and Four-Electron Oxygen Reduction with Cobalt Porphyrin Atropisomers. *Angew. Chem. Int. Ed.* **2021**, *60*, 12742–12746. [[CrossRef](#)]
29. Tong, M.; Sun, F.; Xie, Y.; Wang, Y.; Yang, Y.; Tian, C.; Wang, L.; Fu, H. Operando Cooperated Catalytic Mechanism of Atomically Dispersed Cu-N₄ and Zn-N₄ for Promoting Oxygen Reduction Reaction. *Angew. Chem. Int. Ed.* **2021**, *60*, 14005–14012. [[CrossRef](#)]
30. Côté, A.P.; Benin, A.I.; Ockwig, N.W.; O’Keeffe, M.; Matzger, A.J.; Yaghi, O.M. Porous, crystalline, covalent organic frameworks. *Science* **2005**, *310*, 1166–1170. [[CrossRef](#)]
31. Lin, S.; Diercks, C.S.; Zhang, Y.-B.; Kornienko, N.; Nichols, E.M.; Zhao, Y.; Paris, A.R.; Kim, D.; Yang, P.; Yaghi, O.M.; et al. Covalent organic frameworks comprising cobalt porphyrins for catalytic CO₂ reduction in water. *Science* **2015**, *349*, 1208–1213. [[CrossRef](#)] [[PubMed](#)]
32. Montoro, C.; Rodríguez-San-Miguel, D.; Polo, E.; Escudero-Cid, R.; Ruiz-González, M.L.; Navarro, J.A.R.; Ocón, P.; Zamora, F. Ionic Conductivity and Potential Application for Fuel Cell of a Modified Imine-Based Covalent Organic Framework. *J. Am. Chem. Soc.* **2017**, *139*, 10079–10086. [[CrossRef](#)] [[PubMed](#)]
33. Zhao, X.; Pachfule, P.; Li, S.; Langenhahn, T.; Ye, M.; Schlesiger, C.; Praetz, S.; Schmidt, J.; Thomas, A. Macro/Microporous Covalent Organic Frameworks for Efficient Electrocatalysis. *J. Am. Chem. Soc.* **2019**, *141*, 6623–6630. [[CrossRef](#)] [[PubMed](#)]
34. Li, J.; Jing, X.; Li, Q.; Li, S.; Gao, X.; Feng, X.; Wang, B. Bulk COFs and COF nanosheets for electrochemical energy storage and conversion. *Chem. Soc. Rev.* **2020**, *49*, 3565–3604. [[CrossRef](#)] [[PubMed](#)]
35. Wei, S.; Wang, Y.; Chen, W.; Li, Z.; Cheong, W.-C.; Zhang, Q.; Gong, Y.; Gu, L.; Chen, C.; Wang, D.; et al. Atomically dispersed Fe atoms anchored on COF-derived N-doped carbon nanospheres as efficient multi-functional catalysts. *Chem. Sci.* **2020**, *11*, 786–790. [[CrossRef](#)] [[PubMed](#)]
36. Chen, G.; An, Y.; Liu, S.; Sun, F.; Qi, H.; Wu, H.; He, Y.; Liu, P.; Shi, R.; Zhang, J.; et al. Highly accessible and dense surface single metal FeN₄ active sites for promoting the oxygen reduction reaction. *Energy Environ. Sci.* **2022**, *15*, 2619–2628. [[CrossRef](#)]
37. Du, Z.Z.; Chen, X.J.; Hu, W.; Chuang, C.H.; Xie, S.; Hu, A.J.; Yan, W.S.; Kong, X.H.; Wu, X.J.; Ji, H.X.; et al. Cobalt in Nitrogen-Doped Graphene as Single-Atom Catalyst for High-Sulfur Content Lithium-Sulfur Batteries. *J. Am. Chem. Soc.* **2019**, *141*, 3977–3985. [[CrossRef](#)]

38. Wang, Y.; Arandiyani, H.; Scott, J.; Aguey-Zinsou, K.-F.; Amal, R. Single Atom and Nanoclustered Pt Catalysts for Selective CO₂ Reduction. *ACS Appl. Energ. Mater.* **2018**, *1*, 6781–6789. [[CrossRef](#)]
39. Zhou, Y.; Gu, Q.; Yin, K.; Li, Y.; Tao, L.; Tan, H.; Yang, Y.; Guo, S. Engineering e_g Orbital Occupancy of Pt with Au Alloying Enables Reversible Li-O₂ Batteries. *Angew. Chem. Int. Ed.* **2022**, *61*, e202201416.

Disclaimer/Publisher's Note: The statements, opinions and data contained in all publications are solely those of the individual author(s) and contributor(s) and not of MDPI and/or the editor(s). MDPI and/or the editor(s) disclaim responsibility for any injury to people or property resulting from any ideas, methods, instructions or products referred to in the content.